X-ray wavefront sensor development at the Advanced Light Source

Kenneth Goldberg, Antoine Wojdyla, Diane Bryant, Xianbo Shi, Luca Rebuffi, et al.

Kenneth A. Goldberg, Antoine Wojdyla, Diane Bryant, Xianbo Shi, Luca Rebuffi, Matthew Frith, Matthew Highland, Lahsen Assoufid, Yoshio Ichii, Takato Inoue, Kazuto Yamauchi, "X-ray wavefront sensor development at the Advanced Light Source," Proc. SPIE 12695, Advances in Metrology for X-Ray and EUV Optics X, 126950B (3 October 2023); doi: 10.1117/12.2679136

SPIE.

Event: SPIE Optical Engineering + Applications, 2023, San Diego, California, United States

X-ray wavefront sensor development at the Advanced Light Source

Kenneth A. Goldberg[a,*], Antoine Wojdyla[a], Diane Bryant[a], Xianbo Shi[b], Luca Rebuffi[b], Matthew Frith[b], Matthew Highland[b], Lahsen Assoufid[b], Yoshio Ichii[c], Takato Inoue[d], and Kazuto Yamauchi[e]

[a]Advanced Light Source, Lawrence Berkeley National Laboratory, Berkeley CA 94720, USA
[b]Advanced Photon Source, Argonne National Laboratory, Lemont, IL 60439, USA
[c]JTEC Corporation, 2-4-35 Saito-Yamabuki, Ibaraki, Osaka 567-0086, Japan
[d]Department of Materials Physics, Graduate School of Engineering, Nagoya University, Furo-cho, Chikusa-ku, Nagoya, Aichi 464-8603, Japan
[e]Department of Precision Science and Technology, Graduate School of Engineering, Osaka University, 2-1 Yamada-oka, Suita, Osaka 565-0871, Japan

ABSTRACT

At Lawrence Berkeley National Laboratory's Advanced Light Source, we are developing x-ray wavefront sensors to support the creation and operation of beamlines with diffraction-limited quality. Our new approach to rapid, intermittent wavefront sensing operates in reflection at glancing incidence angles and is compatible with the high-power densities of modern beamlines. For soft x-ray applications especially, the wavefront sensor can operate upstream of the exit slit in a vertically dispersed beam. This single-shot technique supports lateral shearing interferometry and Hartmann wavefront sensing; it can be adapted to speckle-based techniques as well. The reflected beam is directed to an off-axis YAG crystal that produces scintillated visible light. A small mirror reflects the light to a microscope and camera, and the measured wavefront shape information can be used as feedback to adaptive x-ray mirror elements. A compact array of gratings enables measurement across a broad range of photon energies or wavefront curvatures. We describe recent demonstrations at soft x-ray and hard x-ray wavelengths measuring an adaptive x-ray mirror, and a toroidal focusing mirror.

Keywords: X-ray, beamline, wavefront sensor, interferometry, alignment, shearing, Hartmann

1. INTRODUCTION

At x-ray lightsource facilities worldwide, a new generation of beamlines is being created to preserve the extraordinary high source brightness and coherent wavefront properties all the way to the exit slit or sample. These x-ray optical systems must meet demanding performance specifications in order to approach diffraction-limited quality in routine operation. In addition to the coating quality, mirror surface shapes and finish, and the thermal and mechanical stability of optical elements under x-ray power loading are of primary concern.

With advances in mirror fabrication, adaptive x-ray optics, mechanical engineering, and thermal management now enabling the creation of systems that reach these optical quality levels, there is significant attention on wavefront sensing techniques that can be used to perfect the alignment, focusing, and engineered wavefronts these systems require. While it is beneficial to have a variety of complementary feedback modes, we are focusing on at-wavelength, *in situ* wavefront testing for real-time control of mirror alignment and adaptive mirror shapes.

For the Advanced Light Source Upgrade project at Lawrence Berkeley National Laboratory, we have developed a new class of insertable, intermittent, wavefront sensors that operate across a broad range of x-ray wavelengths. Using an off-axis scintillator and viewing system, and glancing angles of incidence on a lithographically fabricated,

Further author information: (Send correspondence to KAG)
E-mail: KAGoldberg@lbl.gov, Telephone: 1 510 495-2261

Advances in Metrology for X-Ray and EUV Optics X, edited by Lahsen Assoufid, Haruhiko Ohashi, Frank Siewert, Proc. of SPIE Vol. 12695, 126950B
 · 0277-786X · doi: 10.1117/12.2679136

patterned grating chip, this technique operates in a minimally invasive mode. The beam is blocked momentarily when in operation, and the grating is removed entirely from the beam when not in use.

Here, we describe the first beamline tests of this wavefront sensor at soft x-ray (SXR) and hard x-ray (HXR) wavelengths. We measured the SXR focusing of a toroidal mirror at the Advanced Light Source, and at HXR wavelengths, we measured an adaptive mirror at the Advanced Photon Source.

2. CURRENT WAVEFRONT-SENSING MODES

A number of different at-wavelength wavefront-sensing approaches are in use worldwide. For HXR wavelengths, there are complementary speckle-based[1–3] and grating-based techniques that use transmission objects and in-line detectors. In the former, a speckle field is generated by a randomly rough, phase-shifting object (e.g. sandpaper, or a lithographically patterned object[4]). The detector images are studied to reveal local displacements of the stable speckle pattern and the underlying wavefront tilts that generated it.

In the two-grating approach (also called *Moiré deflectometry* and *Talbot Interferometry*),[5,6] a first phase grating or amplitude grating projects a fringe pattern onto a second amplitude grating, causing a Moiré effect. With careful, mutual alignment between the gratings, this approach can convert high-spatial-frequency fringes to much lower frequencies that can be measured by an area detector. Translating the second grating laterally produces a "phase-shifting" effect that can be demodulated to improve measurement precision.

High fringe contrast and sensitivity can also be achieved using a single-grating when the grating-to-detector distance is set to a multiple (or a fraction) of the Talbot distance.[7–9] This distance is determined by the wavelength, the grating pitch, and the incident beam's wavefront curvature.

The two-grating and speckle-tracking approaches have been more frequently applied to HXR wavelengths, where penetration depths are higher and high contrast is harder to achieve. However, the single-grating technique can be effective across a range of photon energies.

While these approaches have high efficiency and can be used in a single-shot mode with high sensitivity, there are drawbacks. Transmission gratings and speckle-generating objects in use today invasively block the beam path during measurement. Furthermore, the detector must occupy a straight-ahead, in-line position unless a beam-splitter is used.[10,11] In the two-grating cases, operation across a wide wavelength range may require stages to adjust the longitudinal separation of the grating(s) and the detector plane, adding complexity. In addition, the power density of modern synchrotron and free-electron laser beams is high enough to melt transmission objects in many relevant cases. These challenges motivate our different approach.

3. REFLECTION GRATING CONCEPT

To overcome the beam-blocking problem and mitigate the thermal concerns, we created a single-grating wavefront sensor in reflection geometry. The concept has been described previously by the authors.[12,13] The binary-amplitude reflection grating is patterned onto a silicon wafer chip that is mounted on a platform that *flips* into and out of the beam (Fig. 1), and we call the flipper. By illuminating the grating at glancing angles of incidence and measuring the reflected light downstream, we allow our detector to be positioned off-axis where it does not block the straight-through beam path when the wavefront sensor is not in use.

The gratings are designed to measure the wavefront in one direction as feedback to control adaptive mirrors. As such, the grating patterns run transverse to the beam. With rulings aligned parallel to the direction of propagation, this is commonly called *conical diffraction geometry*. An array of user-selectable gratings allows the grating pitch to be discretely varied. With a fixed grating-to-detector distance, this variation allows the geometry to satisfy the Talbot condition as the operating wavelength changes. The same geometry can be used for converging, parallel, or diverging beams.

The wavefront sensor is intended to operate in the region following the final focusing mirror where converging beam widths range from 0.5 to approximately 4 mm. In the SXR implementation, grating monochromators disperse the beam in one direction upstream of the exit slit. The sensor is oriented to measure the aberrations in the non-dispersed direction.

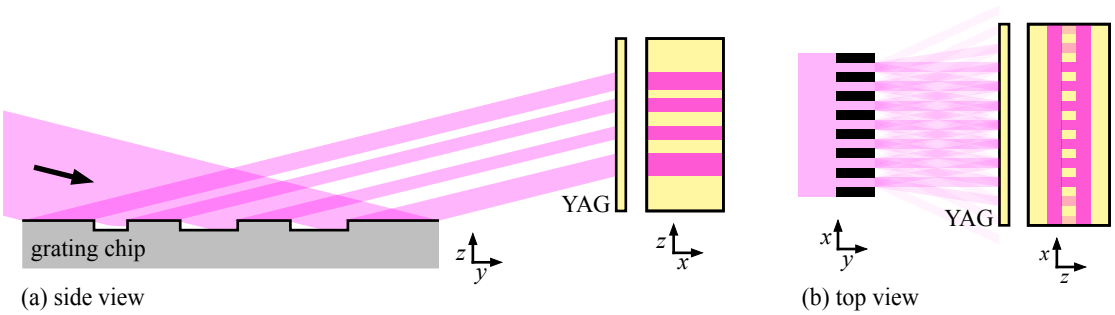

Figure 1: Schematic representations of the reflection grating concept. (a) In side view, from the grating's perspective, light is incident from the left at glancing incidence. Light reflected from the smooth top surface propagates to the YAG (scintillator) and is detected, while light that enters the etched channels is either absorbed in the rough lower surface or reflected into the thick, vertical wall. (b) From the top view, light incident on the patterned region is imprinted with the grating pattern and propagates with diffraction to the detector plane. Where the propagation distance is close to a Talbot-plane distance, a high-contrast fringe pattern will appear.

Our grating is a binary-amplitude reflection grating created with a deep etch, described in Refs. 13 and 12. The features are patterned lithographically onto a silicon wafer chip roughly the size of a postage stamp. (See Fig. 2) A compact array of gratings provides a variety of fixed pitch values to cover an operating energy range that can exceed one decade. The grating is further described in Section 5.

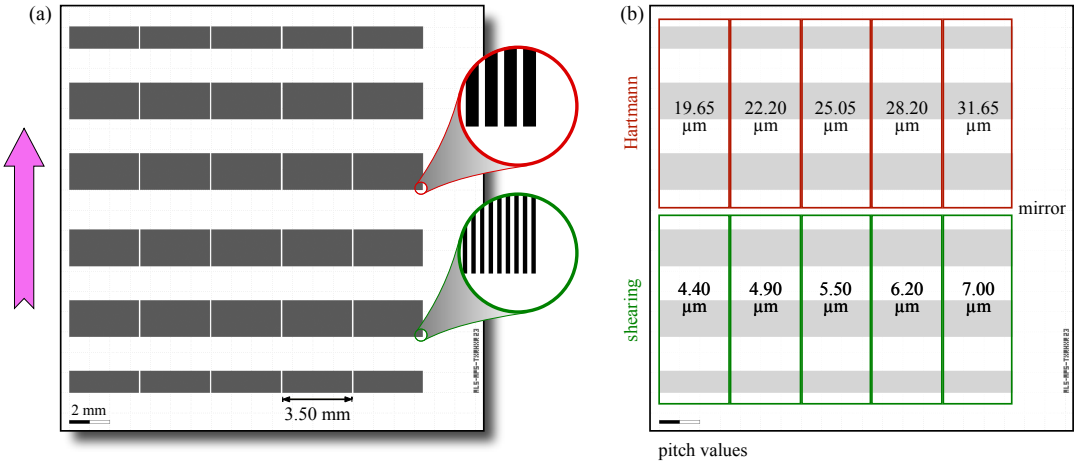

Figure 2: Binary amplitude reflection grating chip layout used for HXR wavefront sensing. The individual grating lines all run vertically. The magenta arrow shows the glancing-incidence illumination direction. The grating regions are separated by reflective, un-etched horizontal obstructions that absorb the unwanted portions of the reflected beam. (a) The grating layout. (b) Annotations indicate the Hartmann grid pitch values (red-boxed regions) and shearing grating pitch values (green boxes). The extended gratings are arranged into 5 columns, in the upper and lower half of the chip. An unpatterned region to the right serves as a mirror for reference. During use, an entire column is illuminated.

Operating at glancing angles of incidence, x-ray mirrors are commonly sized to be hundreds of mm long to capture the entire beam footprint, even for mm-scale beam widths. Since we are probing aberrations only in one direction, our gratings can be significantly shorter, designed to extract only the central portion of the beam cross-section, tens to hundreds of µm across. Surface slope errors in the chip or deformation due to mounting could impact the accuracy of wavefront measurement in a repeatable and systematic way that can be calibrated. Slope errors in the tangential direction will not laterally displace the projected grating patterns. The sensitivity to sagittal slope errors is reduced by the so-called forgiveness factor, $\sin\theta$.

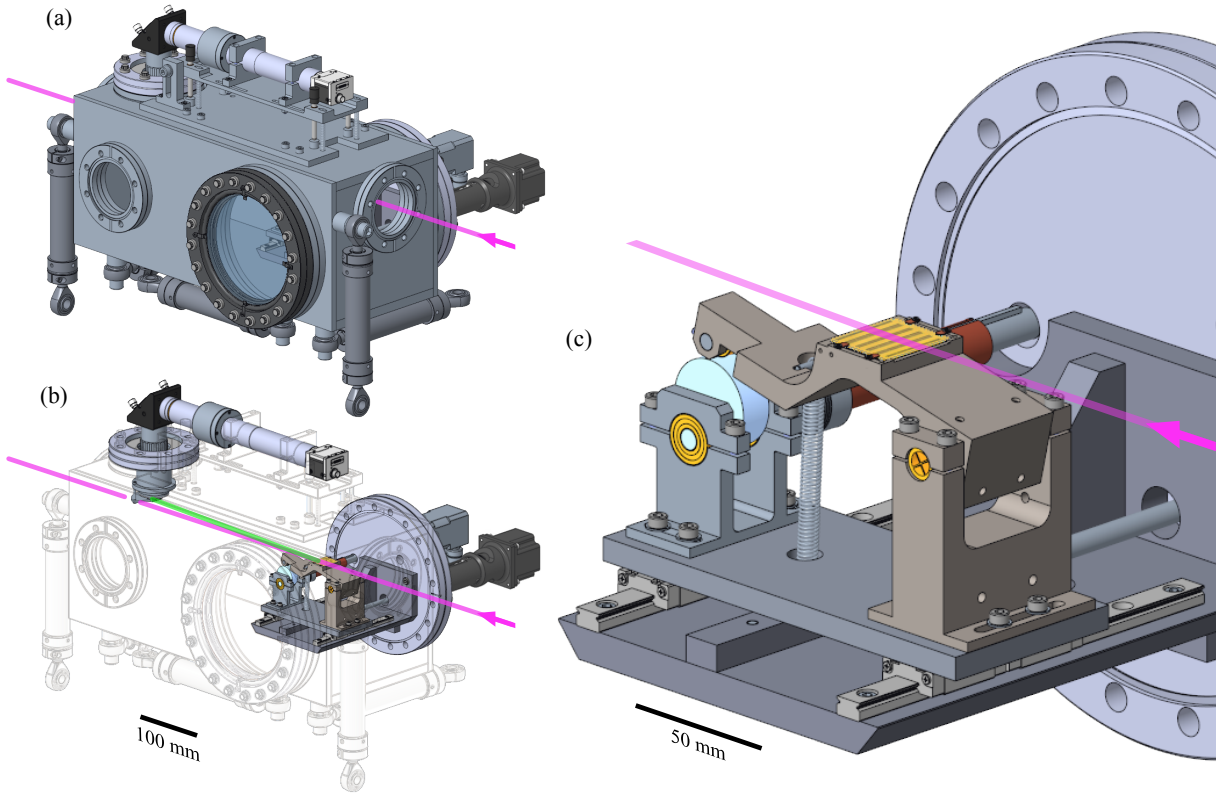

Figure 3: Drawings of the (a) wavefront sensor chamber with attached drives and microscope, (b) the internal components, and (c) a detail of the cam-wheel-driven flipper mechanism and linear stage. With light incident from the right, the straight-through beam path is shown in magenta. When the flipper is in its upward position, the beam is deflected by the grating onto the YAG: this beam path is shown in green. This is the chamber orientation for measuring the wavefront in the horizontal direction.

4. WAVEFRONT SENSOR SYSTEM AND HARDWARE.

The wavefront sensor prototype design described here has become the standard for high-coherent-flux beamlines in the ALS upgrade (ALS-U) project. The chamber is 502 mm long and 225 mm wide, as shown in Fig. 3, not including sealing blanks/windows or mounted mechanical components. Six struts allow manual adjustment of the position and angle while providing mechanical stability. The system shown operates by vertically deflecting the incident x-ray beam. With some modification to the mounting boss locations welded to the chamber, the system can also be rotated on-axis to measure the wavefront in a horizontally-deflecting orientation.

A single 8 inch, customized blank supports the internal mechanical components and their external motors and feedthroughs. The flipper that inserts and retracts the grating is driven by a cam wheel mechanism actuated with a rotary drive. The flipper is connected with a tensioning spring to ensure continuous stable contact with the cam wheel. The lateral position of the grating is adjusted with a motorized linear drive. As the flipper is inserted and retracted, the grating moves vertically by approximately 7 mm.

The grating chip (0.625 mm thick) is mounted in a shallow well machined into the flipper, with a thin piece of indium foil placed underneath to improve thermal contact. The grating chip sits approximately 200 µm proud of the top surface of the flipper and is held in place with several small clips made of thin copper.

With an angle of incidence to the grating set to 1° in the SXR geometry, the center-to-center separation distance between the deflected beam and the straight-through beam path is 10.5 mm at the detection plane. In the HXR geometry, with 0.5° incidence, the distance is reduced to 5.24 mm.

The chamber and its internal components are designed for ultra-high vacuum (UHV) operation; the fully stainless steel chamber operates at or below 1×10^{-7} Torr (1.3×10^{-5} Pa) with a turbo pump.

On beamlines where power loads are expected to exceed several tenths of a Watt, we will improve thermal conduction by using a flexible copper braid that will connect the flipper and its mount. The 8-inch blank has a machined port to accommodate the inclusion of a water-cooled tube that also connects to the flipper mount, providing a complete cooling path.

A 500 µm thick YAG (scintillator) is mounted 300 mm downstream of the grating's central point of intersection. A 5 mm right-angle mirror reflects the light upward into a microscope objective. For compactness and stability, an additional 90° reflection is added to the beam path, outside of the chamber, allowing the imaging camera to be mounted close to the chamber, as shown.

Different objective lenses were used for the SXR and HXR tests based on the required beam width and magnification. The CMOS camera has an array of 4096 × 3000, square pixels with 3.45 µm spacing. With the 2.8× objective, the SXR tests had a maximum field of view of 5.047 mm (limited to below 5 mm by the 45° mirror), and an effective pixel size of 1.232 µm. The HXR tests used a 5.0× objective that provides a 2.862 mm field of view, and 0.690 µm effective pixel size.

5. GRATING PATTERN DESIGN

The chip design process centers around several parameters. Achieving high contrast puts requirements on the etch depth and etched-region length and placement. The operating photon energy range and the measurement geometry dictate the period of the shearing and Hartmann patterns. The total pattern area is constrained by the die size of the 4× deep-ultraviolet lithography process used in the pattern transfer. We further limit the size to 20 mm×18 mm.

The principle of the binary amplitude reflection grating was described previously by the authors.[13] The beam is reflected from the smooth top surface of the chip. Light that enters the etched regions is either absorbed by the rough lower surface, or it is reflected into the vertical wall on the downstream side of the etched region. For an incident glancing angle θ, and etched region length L, the depth a must be greater than $(L/2)\tan\theta$. Our fabrication process typically achieves etch depths exceeding 15 µm depth, but we design for 10 µm to accommodate some variation in the incidence angle.

For HXR use, the longitudinal spacing between grating regions must be substantially larger than the SXR case to ensure that there is sufficient extinction in the unpatterned silicon regions between the grating rows. Furthermore, to increase top-surface reflectivity, the HXR chip was coated with 50 nm of gold.

The design of shearing gratings for single-grating x-ray wavefront sensing—whether in transmission or reflection—centers on the calculation of the optimal grating pitch values. In lateral shearing interferometry, the grating serves as a beam-splitter that produces the coherent interference of overlapping, laterally displaced beams. The most common approach utilizes the Talbot self-imaging effect to produce a high-contrast fringe pattern. The displacement of the fringes reveals the local slope of the wavefront as a discrete derivative that is straightforward to interpret. The beam convergence or divergence affects the Talbot condition and must be accommodated. Several authors have described similar approaches.[12,14,15] For binary amplitude gratings with incident wavelength λ, grating-to-detector-plane distance z, and converging beam radius R (from the grating to focus), we calculate an optimal grating pitch,

$$d = \sqrt{\frac{\lambda z R}{R - z}}. \tag{1}$$

Our convention for the definition of R is shown in Fig. 4. For converging beams $R > 0$, and for diverging beams $R < 0$. In this condition, the fringes observed in the detector plane will have a period that matches the grating, projected geometrically with convergence or divergence onto the detector plane. Note: For collimated beams, we take the limit as $R \to \pm\infty$, and $d = \sqrt{\lambda z}$. For calculation using the photon energy E, we substitute $\lambda = hc/E$. hc is the product of the Plank constant that the speed of light in vacuum, equal to 1239.842 nm/eV.

Equation 1 shows us that the optimal pitch varies with $\sqrt{\lambda}$ or $1/\sqrt{E}$. Therefore, covering a factor of 10 change in photon energy requires gratings with pitch values varying by roughly a factor of 3.

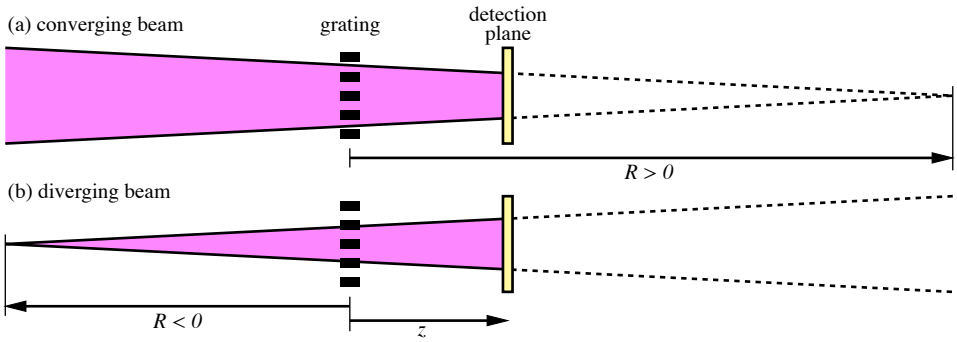

Figure 4: Measurement geometry and definition of terms in the (a) converging beam and (b) diverging beam cases. The beam propagates from left to right.

In the Hartmann test,[16,17] individual beamlets are projected from the grating to the detector without overlapping. The pattern pitch is therefore larger than the shearing case. The width of the openings is chosen to ensure that diffraction does not overlap adjacent beamlets. We have previously described calculations that guide the selection of the width and separation of the openings in the Hartmann grid.[12] Relative to the shearing pitch in Eq. 1, we use a width of $a = 1.5d$ and spacing of $D = 4.5d$.

The grating columns in HXR chip design are 3.5 mm wide with a 75 µm *gutter* region that serves as a visible marker to aid with in-situ positioning. Beam widths in measurement did not exceed 2.0 mm so there was room to translate the grating laterally without encountering the edges.

6. EXPERIMENTAL DEMONSTRATIONS

We describe two beamline measurement campaigns. The first was conducted at the ALS COSMIC beamline's scattering branch at SXR photon energies; the second, at the APS 28-ID beamline, at a fixed 8 keV HXR photon energy.

6.1 Soft x-ray wavefront testing of a toroidal focusing mirror

The ALS COSMIC beamline is powered by an undulator source and uses a variable-included-angle, variable-line space (VIA-VLS) grating monochromator to produce monochromatic SXR light. Downstream of the monochromator's exit slit is a horizontally-deflecting toroidal mirror that produces a two-dimensional focus at the sample position in the endstation. The toroid's object and image distances are 5.0 m and 2.2 m, respectively, and the central angle of incidence is 1.5°. For point-to-point imaging, where an ellipsoidal mirror would be ideal, the toroid is expected to produce a coma aberration with a magnitude that depends on the numerical aperture.

While the reflection angles in the monochromator control the central photon energy downstream, the vertical size of the exit slit controls the illumination bandwidth. The horizontal size controls the width of the intermediate source that illuminates the toroid. For the experiments described here, the energy bandwidth was 0.5%, and the horizontal source size was 4 µm, to filter aberrations from the upstream beamline optics.

We placed the wavefront sensor in the diverging beam behind the sample chamber with the grating chip approximately 1.05 m from focus and measured the horizontal wavefront from the toroidal mirror. At 1° glancing incidence angle on the (vertically deflecting) grating chip, all rows of the grating within a single column are illuminated within the beam and recorded in the detector plane. In fact, the vertical cross-section of the 18 mm tall grating column subtends only 0.314 mm (18 mm × sin 1°) across the beam.

Figure 5 shows several shearing interferogram details, recorded as the photon energy was tuned. This series was designed first to measure the wavefront and then to assess the wavelength dependence of the measurements. Since the toroid's focusing properties are achromatic, we should anticipate a stable, measured wavefront shape, limited by the properties of the reconstruction, when the system (wavelength, grating pitch, and detector-plane distance) is not always optimized for the Talbot condition. The wavefront slope is calculated using the Fourier transform method;[18,19] the slope is numerically integrated to produce the wavefront shape. For measurement,

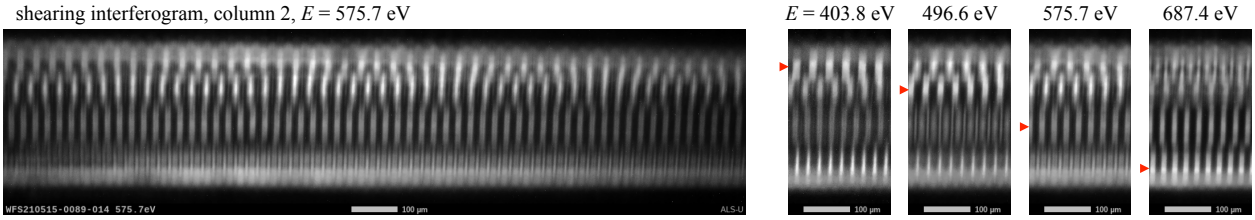

Figure 5: Shearing interferogram details showing four grating regions in one column, illuminated at once. (The column of gratings is represented in Fig. 6.) (Right) An interferogram region 1.578 mm wide. (Left) As the photon energy is tuned, the Talbot condition for high-contrast fringes is met in each of the four rows. The small details are extracted from an energy-tuning series. Red arrows mark the rows with optimal contrast.

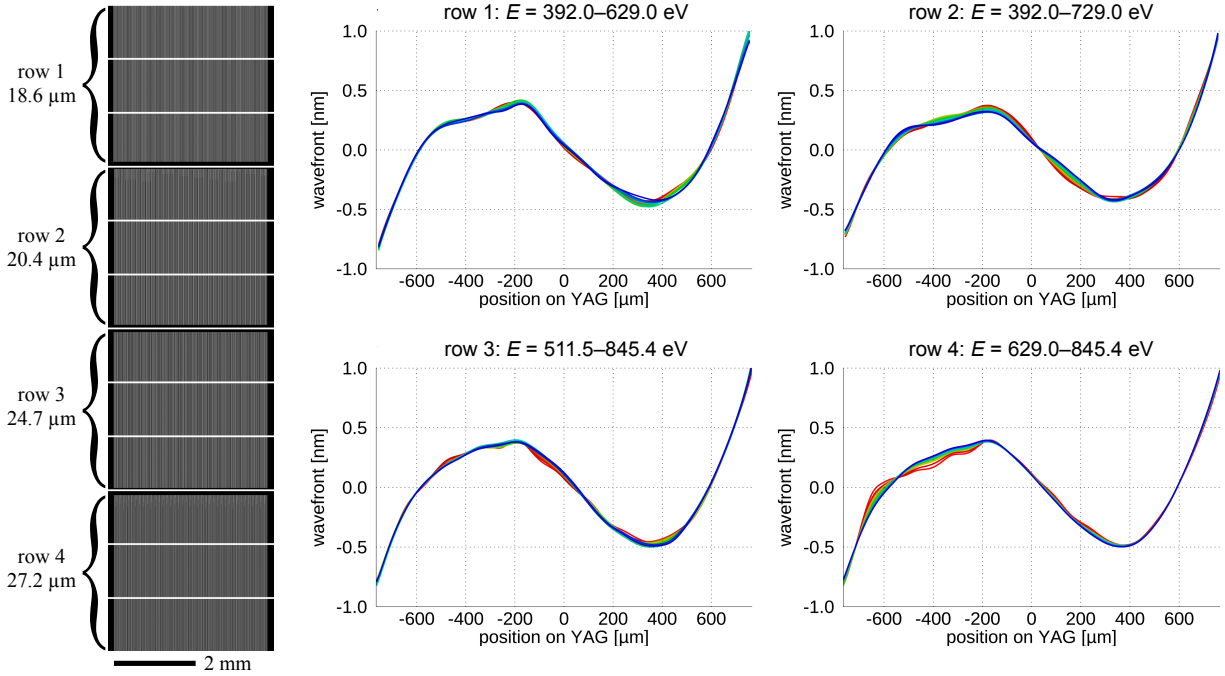

Figure 6: Measured wavefront shapes independently calculated from four gratings, at a range of photon energies. (Left) The grating pattern has four rows of shearing gratings with pitch values shown. Thin horizontal walls in the pattern block reflected light from the etched regions. The photon energy was varied in 27 exponentially increasing steps of 3%, starting from 392.0 eV Within the plots, measurements from multiple photon energies are overlaid, with the range of energies shown in the plot titles. The inherent coma aberration and the achromatic focusing of the toroid are evident.

7 consecutive rows of the camera images are extracted and combined vertically into a 1D intensity array to improve the signal-to-noise ratio. The analyzed wavefront data are shown in Fig. 6, separately for each of the four gratings. In each case, the cylindrical curvature has been removed to reveal the aberrations.

Illuminated at 1.5° incidence, a 1 nm wavefront path length change corresponds to approximately 19.1 nm of surface height change on the mirror. ($\Delta s = 2h \sin\theta$.)[20]

In the measurement series, the photon energy was varied in 27 exponentially increasing, 3% steps, starting at 392.0 eV. The independently extracted wavefronts from each row are overlaid in the plots in Fig. 6. The self-consistency is evident, showing rms variations well within 0.1 nm for each grating, and an overall aberration shape consistency among the four gratings. A detailed performance analysis will be published separately.

We observe that individual gratings can be used over a photon energy range of ±40% photon energy variation when the wavefront aberrations are constrained at this level. This energy range is larger than we expected[12] in

modeling, and deserves further study. We anticipate that the combined influence of the wavefront aberration magnitude (including focal position) and the photon energy change will limit the operating range in practice.

In a VLS monochromator, dispersion causes the apparent source size to blur vertically. Close inspection of Fig. 5 data shows some overlapping between the rows, caused by this effect. Therefore, the gratings must be designed to be long enough to overcome this predictable effect. Otherwise, the interferogram analysis will become more complicated.

6.2 Hard x-ray wavefront testing of an adaptive x-ray optic

The wavefront sensor was tested with a new JTEC adaptive x-ray mirror installed at the Advanced Photon Source's Beamline 28-ID a few weeks before the facility shut down for its upgrade. Our measurements were performed at a fixed 8000 eV photon energy, $\lambda = 0.155$ nm, and showed sensitivity to sub-nanometer actuation of the adaptive mirror.

The adaptive mirror is a 459 mm long, pre-figured tangential ellipse, designed with a nominal $p = 68$ m, $q = 0.46$ m, and $\theta = 3.0$ mrad. The central radius of curvature is approximately 305 m. It is positioned *face-up* in a vertically-deflecting orientation and was illuminated at approximately 3.3 mrad glancing incidence, as shown in Fig. 7. The Si <100> substrate has a 50 nm coating of Pt on the optical surface. For local bending actuation, the mirror has 28 channels running longitudinally along a 380 mm length of the clear aperture. Experiments were performed with a diverging beam.

The wavefront sensor was positioned downstream of the adaptive mirror, rotated on-axis, relative to the SXR orientation, to measure the wavefront variation in the vertical direction. The grating was approximately 812 mm downstream of the mirror center, or 352 mm downstream of the vertical-direction focus, in a diverging beam. This places the detection plane 652 mm from the vertical focus.

In the adaptive mirror, the applied voltage controls the local bending curvature at each channel. In one demonstration, starting from the ground state (0 V applied), channels 13 through 16 were individually actuated with positive and negative 50 V steps. The wavefront differences are plotted in Fig. 8, showing local bending at four different positions. In a second experiment, again starting with the ground state, all channels on the mirror

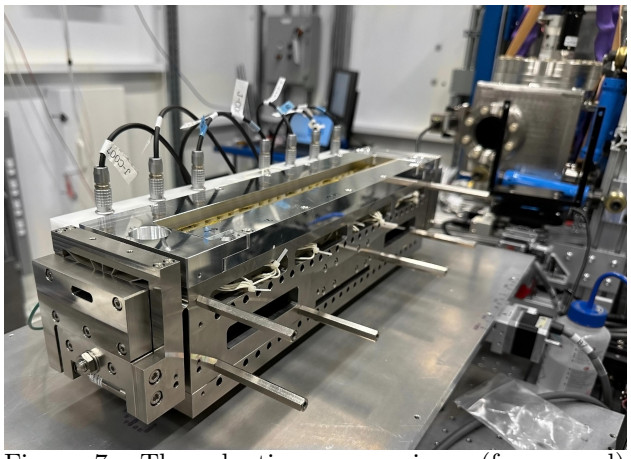

Figure 7: The adaptive x-ray mirror (foreground) and wavefront sensor (background) aligned for testing. Light is incident from the left, and reaches the mirror through the narrow opening. The protective upstream window is removed from the wavefront sensor chamber before measurement.

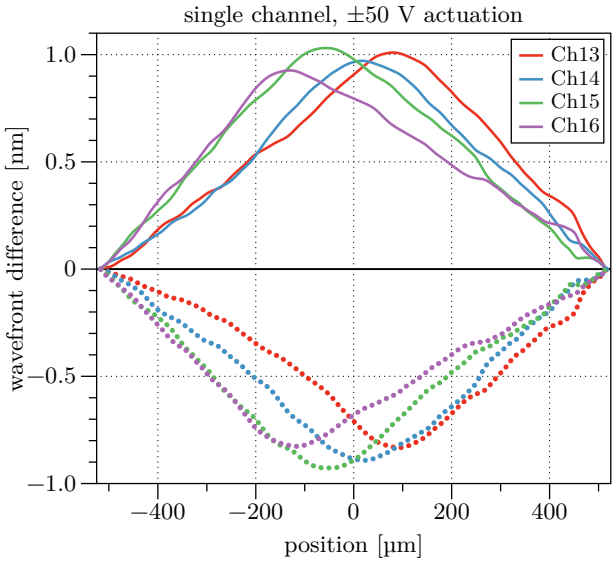

Figure 8: Wavefront difference measurements from the actuation of four individual channels near the center of the mirror. The channels were set from 0 V to +50 V, and then from 0 V to −50 V. As plotted, tilt it removed from the shapes.

were actuated with the same voltage through a series of 7 steps from 1 V up to 64 V, doubling with each step. The measured wavefront differences are shown in Fig. 9. These wavefront differences are plotted as they are measured by the wavefront sensor, with a lateral scaling seen on the detector plane. Given the 3.3 mrad incidence angle, each 1 nm of wavefront path length difference corresponds to a mirror height change of approximately 151.5 nm.

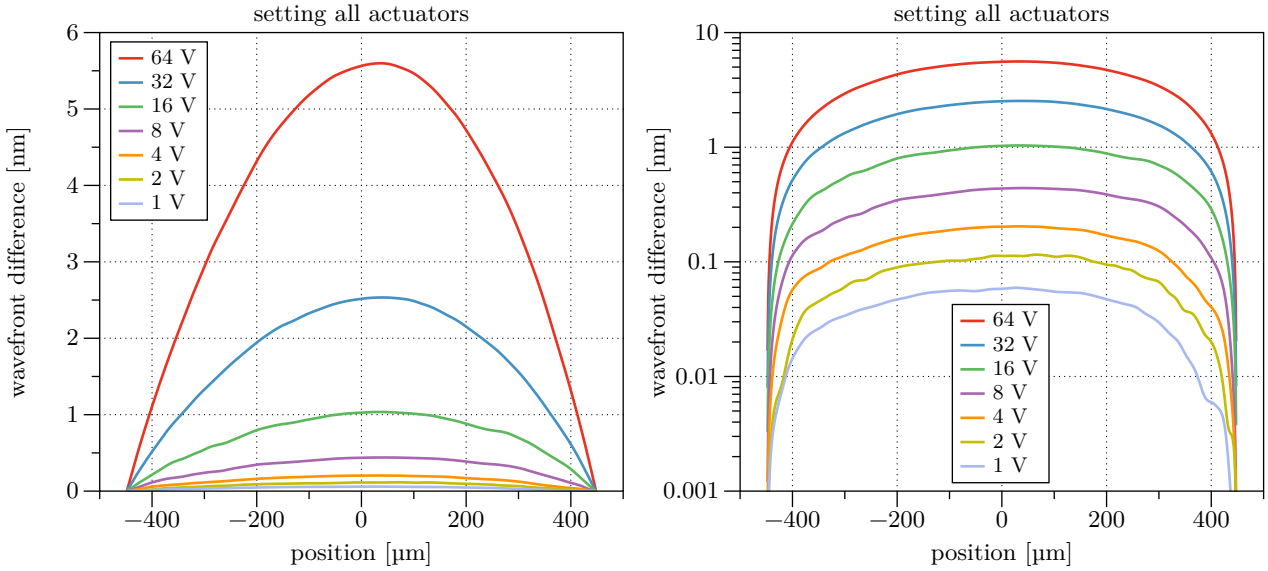

Figure 9: HXR shearing wavefront measurements from the adaptive x-ray mirror recorded at 8000 eV photon energy. All channels are actuated with voltage values increasing from 1 V to 64 V, doubling with each step. Relative to the ground state shape, measured wavefront differences are shown in (left) linear and (right) logarithmic scaling. The lateral position values represent the wavefront positions in the detection plane.

7. CONCLUSION

Rapid wavefront sensing feedback is essential for the control of adaptive optics on high-coherent-flux x-ray beamlines. Working at SXR and HXR photon energies, we have demonstrated a new reflective approach to wavefront sensing that we describe as *intermittent* or *minimally invasive*. During operation, the glancing-incidence grating array is inserted momentarily, and when it is retracted, the beam resumes its unobstructed path. This geometry mitigates concerns about the power density on normal-incidence gratings patterned on thin membranes or structures.

Our design includes a compact array of one-dimensional gratings to accommodate a wide range of photon energies or wavefront curvatures when measuring using the single-grating shearing or the Hartmann approach. One-dimensional measurement provides the required feedback for the current generation of adaptive mirrors. The system can measure beams as narrow as a few tenths of a mm.

We have shown that the measurements remain stable as the photon energy is tuned through a broad range (∼40%), and that they are sensitive to sub-tenth-nm variations in the wavefront shape.

The extension of this approach to speckle-tracking mode should be straightforward with a naturally random or a programmed, patterned surface. Furthermore, a longer grating array would enable wavefront measurement in two dimensions to be achieved.

ACKNOWLEDGMENTS

The authors are indebted to Sophie Morley and Sujoy Roy for their kind support and expert assistance at the ALS COSMIC beamline. We appreciate the support and guidance of Eliane DiMasi, Howard Padmore, and Andreas Scholl. AMFitzgerald produced the grating chips for both sets of experiments. The Advanced Light Source is supported by the Director, Office of Science, Office of Basic Energy Sciences, of the U.S. Department

of Energy under Contract No. DE-AC02-05CH11231. The Advanced Photon Source is supported by the U.S. Department of Energy, Office of Science, Office of Basic Energy Sciences, under contract DE-AC02-06CH11357. The adaptive optics development was supported by JSPS KAKENHI Grant Number JP21H05004.

REFERENCES

[1] Bérujon, S., Ziegler, E., Cerbino, R., and Peverini, L., "Two-dimensional x-ray beam phase sensing," *Physical Review Letters* **108**, 1–5 (04 2012).

[2] Berujon, S., Ziegler, E., and Cloetens, P., "X-ray pulse wavefront metrology using speckle tracking," *Journal of Synchrotron Radiation* **22**, 886–894 (07 2015).

[3] Kashyap, Y., Wang, H., and Sawhney, K., "Speckle-based at-wavelength metrology of X-ray mirrors with super accuracy," *Review of Scientific Instruments* **87**, 052001 (05 2016).

[4] Qiao, Z., Shi, X., Wojcik, M. J., Rebuffi, L., and Assoufid, L., "Single-shot x-ray phase-contrast and dark-field imaging based on coded binary phase mask," *Applied Physics Letters* **119**, 011105 (07 2021).

[5] Momose, A., Kawamoto, S., Koyama, I., Hamaishi, Y., Takai, K., and Suzuki, Y., "Demonstration of x-ray talbot interferometry," *Japanese Journal of Applied Physics* **42**, L866 (07 2003).

[6] Weitkamp, T., Nöhammer, B., Diaz, A., David, C., and Ziegler, E., "X-ray wavefront analysis and optics characterization with a grating interferometer," *Applied Physics Letters* **86**, 054101 (01 2005).

[7] Naulleau, P. P., Goldberg, K. A., and Bokor, J., "Extreme ultraviolet carrier-frequency shearing interferometry of a lithographic four-mirror optical system," *Journal of Vacuum Science & Technology B* **18**, 2939–2943 (11 2000).

[8] Hasegawa, M., Ouchi, C., Hasegawa, T., Kato, S., Ohkubo, A., Suzuki, A., Sugisaki, K., Okada, M., Otaki, K., Murakami, K., Saito, J., Niibe, M., and Takeda, M., "Recent progress of EUV wavefront metrology in EUVA," *Proc. SPIE* **5533**, 27–36 (2004).

[9] Matsuyama, S., Yokoyama, H., Fukui, R., Kohmura, Y., Tamasaku, K., Yabashi, M., Yashiro, W., Momose, A., Ishikawa, T., and Yamauchi, K., "Wavefront measurement for a hard-x-ray nanobeam using single-grating interferometry," *Opt. Express* **20**, 24977–24986 (Oct 2012).

[10] Goldberg, K. A., Wojdyla, A., Bryant, D., Chao, W., Cocco, D., Hardin, C., Morton, D., Ng, M. L., Lee, L., Assoufid, L., Grizolli, W., Shi, X., Kearney, S. P., Wojcik, M., Shvyd'ko, Y., Shu, D., Idir, M., and Huang, L., "Collaborative development of diffraction-limited beamline optical systems at US DOE light sources," *Proc. SPIE* **11109**, 111090C (2019).

[11] Shi, X., Qiao, Z., Rebuffi, L., Wojcik, M., Highland, M., Frith, M. G., Harder, R., Shu, D., Mashrafi, S., Anton, J., Kearney, S., Wyman, M., and Assoufid, L., "Development of x-ray wavefront sensing techniques for adaptive optics control at the advanced photon source," *Synchrotron Radiation News* **35**(2), 37–42 (2022).

[12] Goldberg, K. A., Wojdyla, A., and Bryant, D., "Binary Amplitude Reflection Gratings for X-ray Shearing and Hartmann Wavefront Sensors," *Sensors* **21**, 536 (01 2021).

[13] Goldberg, K. A., Bryant, D., Wojdyla, A., Helmbrecht, M., and Gullikson, E., "Reflective binary amplitude grating for soft x-ray shearing and Hartmann wavefront sensing," *Optics Letters* **45**, 4694 (09 2020).

[14] Merthe, D. J., Yashchuk, V. V., Goldberg, K. A., Kunz, M., Tamura, N., McKinney, W. R., Artemiev, N. A., Celestre, R. S., Morrison, G. Y., Anderson, E. H., Smith, B. V., Domning, E. E., Rekawa, S. B., and Padmore, H. A., "Methodology for optimal in situ alignment and setting of bendable optics for nearly diffraction-limited focusing of soft x-rays," *Optical Engineering* **52**(3), 033603 (2013).

[15] Seaberg, M., Cojocaru, R., Berujon, S., Ziegler, E., Jaggi, A., Krempasky, J., Seiboth, F., Aquila, A., Liu, Y., Sakdinawat, A., Lee, H. J., Flechsig, U., Patthey, L., Koch, F., Seniutinas, G., David, C., Zhu, D., Mikeš, L., Makita, M., Koyama, T., Mancuso, A. P., Chapman, H. N., and Vagovič, P., "Wavefront sensing at X-ray free-electron lasers," *Journal of Synchrotron Radiation* **26**, 1115–1126 (07 2019).

[16] Mercère, P., Zeitoun, P., Idir, M., Le Pape, S., Douillet, D., Levecq, X., Dovillaire, G., Bucourt, S., Goldberg, K. A., Naulleau, P. P., and Rekawa, S., "Hartmann wave-front measurement at 13.4 nm with $\lambda_{\mathrm{EUV}}/120$ accuracy," *Optics Letters* **28**(17), 1534 (2003).

[17] Mercère, P., Bucourt, S., Cauchon, G., Douillet, D., Dovillaire, G., Goldberg, K. A., Idir, M., Levecq, X., Moreno, T., Naulleau, P. P., Rekawa, S., and Zeitoun, P., "X-ray beam metrology and x-ray optic alignment by Hartmann wavefront sensing," *Proc. SPIE* **5921**, 592109 (2005).

[18] Takeda, M., Ina, H., and Kobayashi, S., "Fourier-transform method of fringe-pattern analysis for computer-based topography and interferometry," *Journal of the Optical Society of America* **72**, 156–160 (01 1982).

[19] Servin, M., Cywiak, M., and Dávila, A., "Lateral shearing interferometry: theoretical limits with practical consequences," *Opt. Express* **15**, 17805–17818 (12 2007).

[20] Goldberg, K. A. and Yashchuk, V. V., "Optimized mirror shape tuning using beam weightings based on distance, angle of incidence, reflectivity, and power," *Review of Scientific Instruments* **87**, 051805 (05 2016).